U–Pb and Ar–Ar geochronology of the Fujiawu porphyry Cu–Mo deposit, Dexing district, Southeast China: Implications for magmatism, hydrothermal alteration, and mineralization

Xiaofeng Li [a,*], Ruizhong Hu [a], Brian Rusk [b], Rong Xiao [c], Cuiyun Wang [d], Feng Yang [d]

[a] State Key Laboratory of Ore Deposit Geochemistry, Institute of Geochemistry, Chinese Academy of Sciences, Guiyang, Guizhou 550002, China
[b] Western Washington University, Bellingham, WA, USA
[c] Hunan Institute of Geological Survey, Changsha 410116, China
[d] Guilin University of Technology, Guilin 541004, China

A B S T R A C T

The Fujiawu porphyry Cu–Mo deposit is one of several porphyry Cu–Mo deposits in the Dexing district, Jiangxi Province, Southeast China. New zircon SHRIMP U–Pb data yield a weighted mean $^{206}Pb/^{238}U$ age of 172.0 ± 2.1 and 168.5 ± 1.4 Ma from weakly altered granodiorite porphyry and quartz diorite porphyry, respectively. Two hydrothermal biotites from granodiorite porphyry give an Ar–Ar step-heating plateau age of 169.9 ± 1.8 and 168.7 ± 1.8 Ma. Hydrothermal apatite exsolved from altered biotite yields an isotope dilution thermal ionization mass spectrometry isochron age of 164.4 ± 0.9 Ma. The apatite age is similar to the ages obtained from hydrothermal rutile (165.0 ± 1.1 and 164.8 ± 1.6 Ma) and indicates that the magmatism and hydrothermal activity in the Fujiawu deposit occurred in the Middle Jurassic. Hydrothermal fluid circulation related to multiple stages of magma emplacement resulted in Cu–Mo mineralization in the Fujiawu porphyry deposit. The zircon SHRIMP U–Pb ages and the published molybdenite Re–Os age (170.9 ± 1.5 Ma) represent the timing of magma crystallization and Mo mineralization, whereas the rutile and apatite U–Pb ages reflect the timing of Cu mineralization following quartz diorite emplacement. The data suggest slow cooling after emplacement of the quartz diorite porphyry.

© 2013 Elsevier Ltd. All rights reserved.

1. Introduction

The Dexing porphyry Cu–Mo district in Jiangxi Province, Southeast China, comprises three important porphyry Cu deposits: the Tongchang, Zhushahong, and Fujiawu deposits (Figs. 1 and 2). The assemblages, zoning, and paragenesis of the hydrothermal minerals of the Dexing porphyry district and the origin and the evolution of the mineralized porphyry system have long been studied. The history of the exploration, study, and present understanding of the origin of porphyry deposits have been reviewed by Zhu et al. (1983), Hua et al. (2000), Rui et al. (2005), and Li et al. (2012) (and see references therein). Owing to extensive hydrothermal alteration, the available Rb–Sr and K–Ar ages of the porphyries are unreliable and fall in a wide range from 193 to 112 Ma (Zhu et al., 1983; Rui et al. 1984), but the Middle Jurassic ages for magma emplacement and Mo mineralization have been accepted since the works of Wang et al. (2006) and Lu et al. (2005). However, most

earlier studies in this district have focused on the Tongchang deposit (Zhu et al., 1983; Wang et al., 2006; Li and Sasaki, 2007), and only a few studies have been conducted on the Zhushahong and Fujiawu deposits (Wang et al., 2012). The duration of economic ore formation is therefore poorly defined.

To better understand the timing of mineralization and hydrothermal events in the Dexing porphyry Cu–Mo deposit, the current study focuses on the Fujiawu deposit, the eastern portion of the Dexing porphyry Cu–Mo district, but is relevant to the other Dexing deposits. In this paper, we present new geochronological results including zircon SHRIMP U–Pb ages and the first hydrothermal biotite Ar–Ar ages, as well as rutile and apatite isotope dilution thermal ionization mass spectrometry (ID-TIMS) U–Pb ages. The integration of these techniques provides rigorous geochronologic constraints on magma emplacement and the duration of hydrothermal alteration and mineralization. These new age data lead us to conclude that the Fujiawu Cu–Mo deposit is the product of multiple stages of magma emplacement, hydrothermal activity, and Cu–Mo mineralization, lasting for 6–7 million years. Mo mineralization occurred soon after magma emplacement, whereas Cu mineralization occurred 6 to 7 years later suggesting multiple pulses of magmatic hydrothermal fluids in a slowly cooling hydrothermal system.

* Corresponding author. Address: Institute of Geochemistry, Chinese Academy of Sciences, 46 Guanshui Road, Guiyang, Guizhou 550002, China. Tel.: +86 851 5891199.
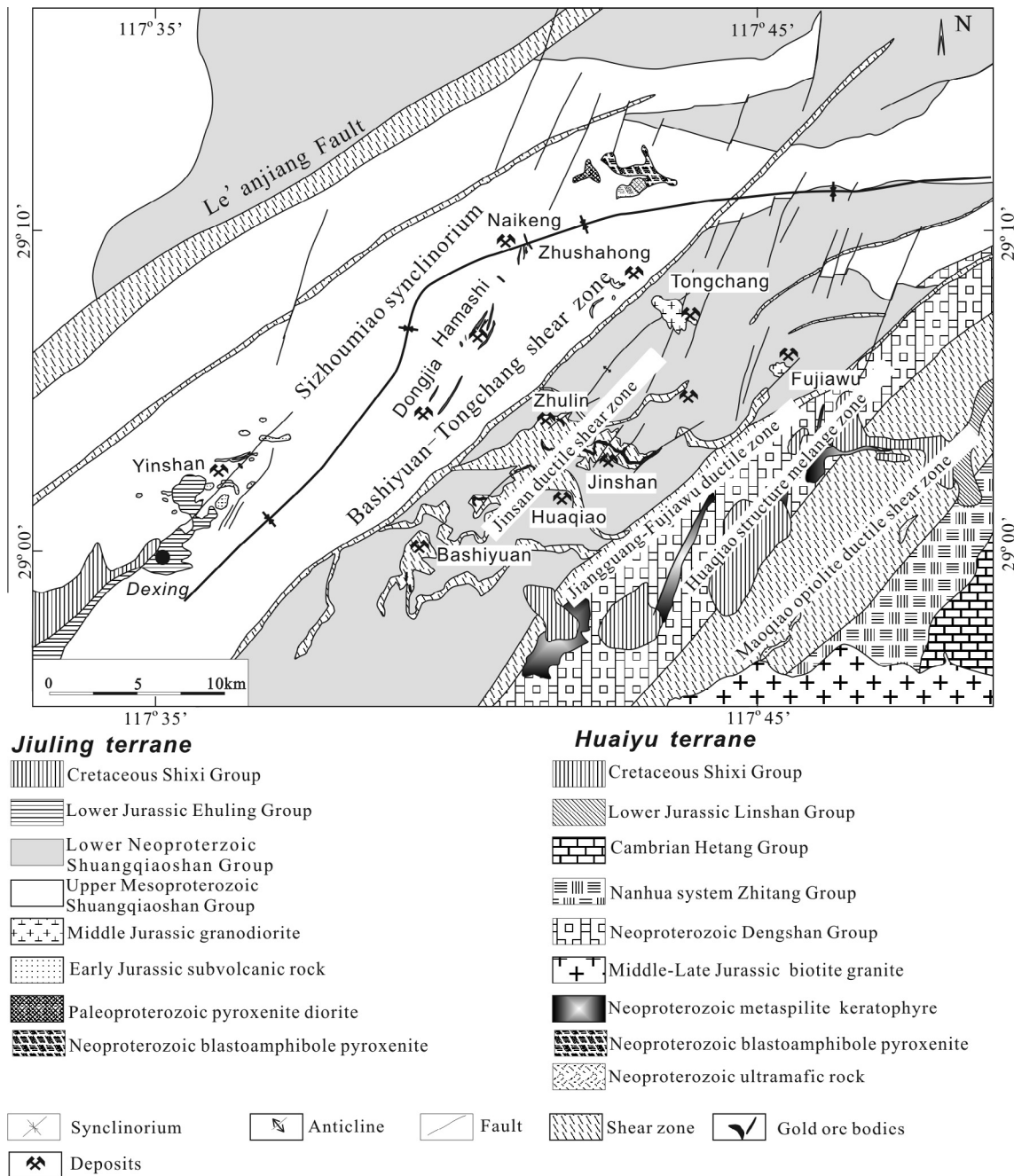E-mail address: x-f-li@hotmail.com (X. Li).

Fig. 1. Regional geological map of Dexing porphyry Cu–Mo district, Jiangxi Province, Southeast China (After Li et al., 2010).

2. Regional geology setting

The Fujiawu porphyry Cu deposit lies in the eastern Jiangnan Orogenic Belt in northeastern Jiangxi Province, which lies between the Yangtze craton and the Cathaysian craton (Li and Sasaki, 2007). It is a part of the Mesozoic magmatic belt in the Jiangnan tectonic belt. The Jiangnan Orogenic Belt is composed of low-grade metamorphosed sedimentary rocks and mafic volcanic rocks of the Neoproterozoic Shuangqiaoshan Group. It records a multistage Late Proterozoic collision (Guo et al., 1980; Zhou and Zhu, 1993; Charvet et al., 1996) between the Huaiyu terrane in the southeast and the Jiuling terrane in the northwest (Shu et al., 1995). The Jiuling terrane is composed predominantly of Middle to Late Proterozoic continent-derived flysch turbidites and littoral sedimentary rocks. The southern flysch contains mafic and ultramafic intrusives dated

at 1515 ± 241 Ma (Shu, 1991). The Huaiyu terrane consists of Middle–Late Proterozoic metavolcanic rocks, including turbiditic flysch and ophiolitic mélange dated at 930–1000 Ma (Shu, 1991). Metavolcanic rocks in the Huaiyu terrane are mainly Middle Proterozoic basalt and diabase as well as Late Proterozoic basalt, andesite, and rhyolite (Shu, 1991). The collision of these two terranes resulted in regional shortening and folding, greenschist-facies metamorphism, and the intrusion of felsic plutons in the Neoproterozoic (891–913 Ma, zircon SHRIMP U–Pb) (Shu, 2012).

The suture between the Huaiyu and Jiuling terranes is marked by a northeast-trending regional deep crustal fault system, the Northeast Jiangxi Deep Fault (NJDF) (Fig. 1). The steeply northwest dipping NJDF is the dominant linear tectonic feature along the Jiangnan Orogenic Belt. It is 10–20 km wide and at least 200 km long. The NJDF is characterized by a 4- to 5-km-wide ophiolite and
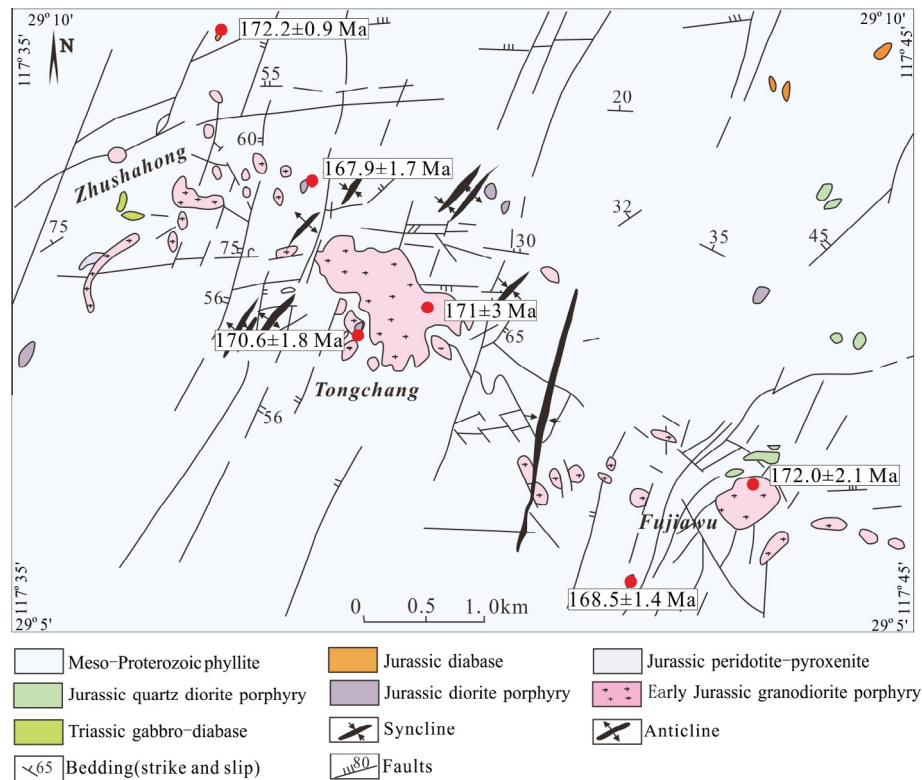
Fig. 2. Geological map of the Fujiawu porphyry Cu–Mo deposit including lithologic units and major structures. The red spots are the sample sites for zircon SHRIMP U–Pb age dating.

mélange sequence and includes the ductilely sheared Maoqiao ophiolite and the Huaqiao mélange zones (Fig. 1). The NJDF was reactivated as a reverse fault during the Caledonian and Indo-China orogenies and extension in the Yanshanian orogeny resulted in a series of red-bed basins (Shu et al., 1995).

The Jiangnan Orogenic Belt was intruded by Late Permian–Triassic peraluminous granites and alkaline syenite (Li and Sasaki, 2007), as well as Jurassic and Cretaceous ilmenite series granitoids and gabbroic rocks (Zhou and Li, 2000). These magmatic activities are attributed to the northwestward subduction of the Paleo-Pacific plate beneath the Cathaysian–Yangtze craton (Zhou and Li, 2000; Zhou et al., 2006), or to subduction in an intraplate setting (Hu et al., 1992), or to ridge subduction beneath the Cathaysian–Yangtze craton (Li et al., 2008).

3. Geology of the Fujiawu Cu–Mo deposit

The Fujiawu porphyry deposit is situated southeast of the Tongchang deposit between the NNE-trending Le'anjing and Northeast Jiangxi faults (Fig. 1). Porphyry Cu–Mo mineralization in the Dexing district is mainly associated with Jurassic granodiorite porphyry and quartz diorite porphyry (Zhu et al., 1983). They occurred as comagmatic multiphase intrusive complexes comprising, from earlier to later, diorite, granodiorite porphyry, quartz diorite porphyry, potassic feldspar granite, and diabase dikes (Zhu et al., 1983). Magmatism and mineralization at the Tongchang, Zhushahong, and Fujiawu deposits are structurally controlled by NW-trending, E–W-trending, and NE-trending fault sets. The granodiorite porphyries dated at 171 Ma (Wang et al., 2006) intruded metamorphic volcanic–sedimentary rocks of the Shuangqiaoshan Group. The Zhushahong, Tongchang, and Fujiawu porphyry stocks are oriented at 300° with a slight leftward

displacement from one another. They plunge 40–70° to the NW. The Fujiawu porphyries occur as isolated pipelike stocks with outcrops of 0.2 km². These intrusive bodies are cut by NNE-striking left-lateral faults (Fig. 2). The Cu–Mo mineralization at Fujiawu is both vein-hosted and disseminated, and it is concentrated along fractures at the contact zone between the granodiorite and the Shuangqiaoshan phyllite (Fig. 3a). Two thirds of the identified ore bodies occur in the phyllite of the Shuangqiaoshan Group (Fig. 3b). The dominant Cu mineral is chalcopyrite (>90%), with lesser amounts of bornite, tetrahedrite, and chalcocite.

Alteration and mineralization in the Fujiawu porphyry Cu–Mo deposit have not been previously well documented but can be divided into four stages following the terminology of Gustafson and Hunt (1975) and Li and Sasaki (2007). Vein types include early, largely barren A veins with K-feldspar alteration, transitional B veins with chlorite–illite alteration, later D veins with phyllic (quartz + muscovite) alteration, and the latest H veins with carbonate + sulfate + hematite alteration (Fig. 4). The A veins consist of granular quartz + K-feldspar plus minor amounts of sulfides, or K-feldspar veins, or quartz + magnetite + K-feldspar ± chalcopyrite (Fig. 4a). The transitional B veins are characterized by quartz + molybdenite with minor amounts of chalcopyrite or quartz + molybdenite (Fig. 4b). B veins are inferred to have formed in the transition from K-feldspar-stable to K-feldspar-destructive conditions. Later D veins are characterized by abundant pyrite and chalcopyrite (Fig. 4c) and alteration of K-feldspar to muscovite and quartz and of mafic minerals to pyrite and rutile. D veins contain the bulk of the ore as chalcopyrite in addition to quartz and most host muscovite and/or chlorite alteration. The latest hydrothermal event is characterized by carbonate + pyrite alteration and contains hematite and chalcopyrite (Fig. 4d and e). Zhu et al. (1983) suggest that chalcopyrite mineralization occurred between 350 °C and 200 °C during quartz-muscovite alteration, likely as fluids cooled.
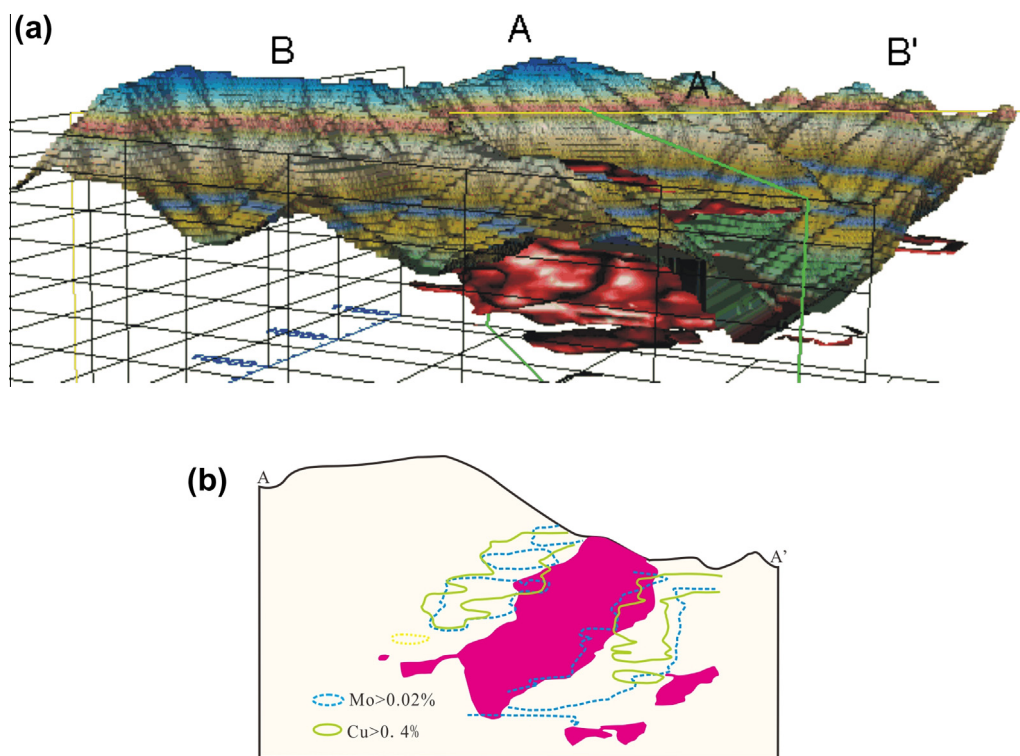
Fig. 3. Mine scale distribution of Cu, Au and Mo in the Fujiawu deposit, based on three-dimensional modeling data from Fujiawu mine coordinates (m). Orientations in text are referenced to True North and elevation is meters above sea level. (a) Three dimensional views on the Fujiawu deposit, looking southeast. Shown are the original topography (gray surface) and the envelope surface of >0.35 wt% Cu (red bodies). Orientations of cross sections are indicated. (b)Vertical northwest–southeast cross section (A–A′), showing Cu grade together with contours of MoS_2 concentration, respectively.

Multistage veins were overprinted by late veins were also observed at Fujiawu deposit (Fig. 4e and f).

4. Age sampling and analytical methods

4.1. Sample description

Samples FJW-19 and FJW-20 were collected in the Fujiawu open pit, and sample FJW-8 was collected 500 m southwest of the open pit. Samples FJW-19 and FJW-20 are weakly K-feldspar-altered granodiorite porphyry (Fig. 5a and b) and sample FJW-8 is sericite-altered quartz diorite porphyry. The descriptions for each sample follow.

4.1.1. Sample FJW-19

This sample consists of K-feldspar-altered granodiorite porphyry with disseminated Cu mineralization (Fig. 5a). Phenocrysts are dominated by euhedral plagioclase (26%), platy biotite (6%), hornblende (2%), and quartz (6%) with minor amounts of apatite and orthoclase. The groundmass is composed of quartz (16%), K-feldspar (20%), plagioclase (10%), biotite (5%), and hornblende (4%). Accessory minerals include apatite and magnetite with trace zircon and rutile. The plagioclase in phenocrysts and groundmass are replaced by K-feldspar. Some plagioclase is also slightly altered to kaolinite, sericite, and muscovite. Shreddy biotite (0.2–2.5 mm) is slightly altered to chlorite and epidote. Igneous apatite grains occur as columns up to 0.5 × 0.5 mm enclosed in plagioclase grains. Hydrothermal magnetite, apatite, and needle-like rutile that exsolved from some biotite occurred along the cleavages (Fig. 5c). Some granular magnetite grains have hematite margins and some orthoclase is slightly altered to kaolinite. Disseminated chalcopyrite is replaced and surrounded by chalcocite at the rim. The sample

is cut by hydrothermal quartz + sulfide (pyrite + chalcopyrite) + rutile "D" veins (Fig. 5d). In sample FJW-19, two types of rutile are present: needle-like rutile exsolved from biotite and granular rutile found within the quartz + sulfide veins.

4.1.2. Sample FJW-20

This sample consists of weakly K-feldspar-altered granodiorite porphyry with disseminated Cu mineralization (Fig. 5b). Phenocrysts are dominated by euhedral plagioclase (20%), platy biotite (5%), hornblende (2%), and quartz (7%) with minor amounts of apatite and orthoclase. The groundmass is composed of quartz (18%), K-feldspar (25%), plagioclase (8%), biotite (4%), and hornblende (3%). Accessory minerals include apatite and magnetite, with trace amounts of zircon and rutile (Fig. 5e).

The plagioclase in phenocrysts and groundmass are replaced by K-feldspar. Some plagioclase is also slightly altered to kaolinite and sericite. Shreddy biotite (0.2–2.5 mm) is slightly altered to chlorite and epidote. Hydrothermal magnetite and needle-like rutile were exsolved from biotite. Igneous apatite grains occur as columns up to 0.5 × 0.5 mm enclosed in plagioclase grains (Fig. 5f). Some granular magnetite grains have hematite margins and some orthoclase is slightly altered to kaolinite. Disseminated chalcopyrite is replaced by and surrounded by chalcocite at the rim. The sample was cut by thin pyrite veins.

4.1.3. Sample FJW-8

This sample consists of sericite-altered quartz diorite porphyry with no Cu–Mo mineralization. Phenocrysts are dominated by euhedral plagioclase (30%), platy biotite (5%), hornblende (5%), and quartz (2%) with a minor amount of apatite (1%). The groundmass is composed of quartz (18%), K-feldspar (25%), plagioclase (8%), and minor amounts of biotite and hornblende (3%). Accessory
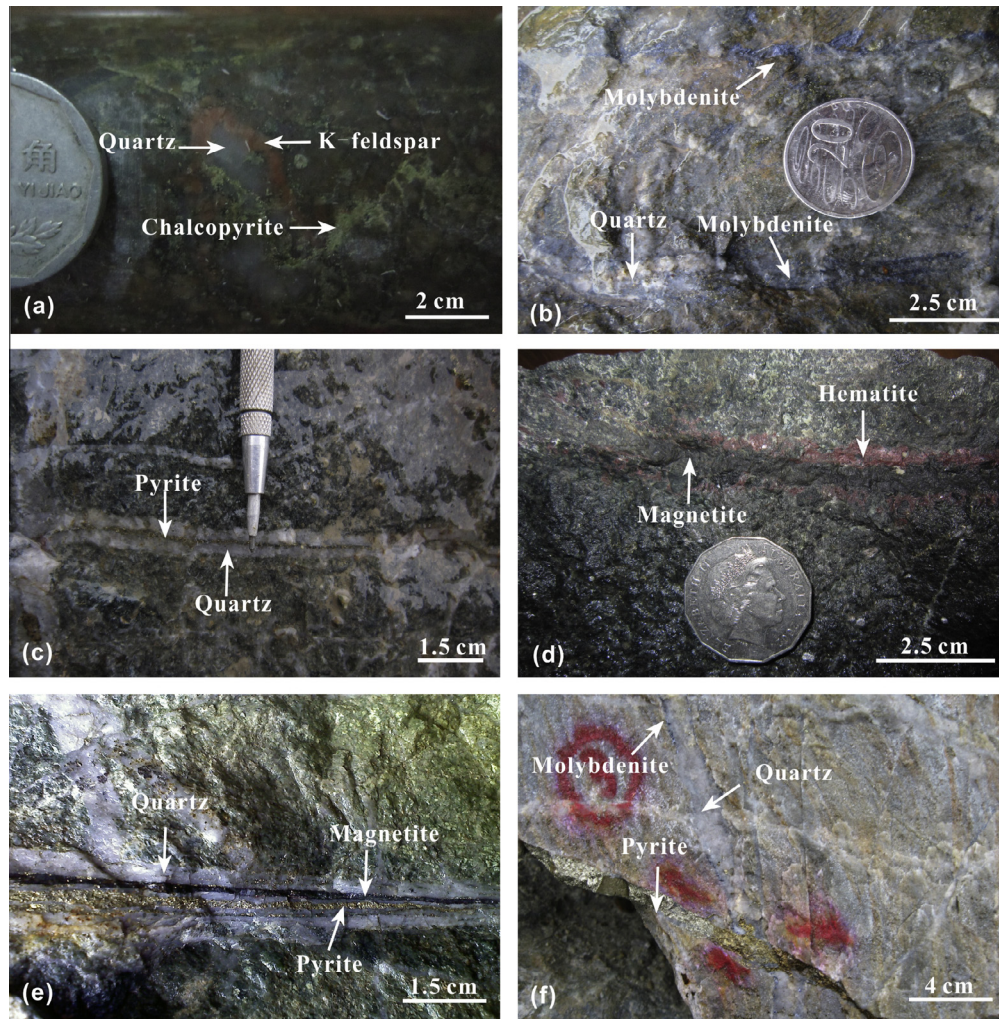
Fig. 4. Photographs of veins and wall-rock alteration in Fujiawu. All samples are from open pit exposures except photograph A from drill hole FZK6-1. (a) A quartz + K-feldspar + chalcopyrite vein in granodiorite porphyry in drill hole FZK6-1. (b) A quartz + molybdenite vein cut by a later carbonate vein in level 320. (c) Quartz + pyrite vein in granodiorite porphyry in level 320. (d) Magnetite vein with hematite margin. (e) Quartz + pyrite vein cut by later hematite vein. (f) Multistage veins in granodiorite. The earlier quartz + molybdenite vein was cut by a late quartz + pyrite vein.

minerals include apatite and magnetite, with trace amounts of zircon and rutile. Plagioclase is altered to sericite, and biotite and hornblende are altered to chlorite and sericite.

4.2. Zircon SHRIMP U–Pb geochronology

We selected zircon grains from sample FJW-19 and FJW-8. Conventional crushing and grinding techniques were used to concentrate zircon crystals smaller than 0.2 mm before manual heavy liquid rinsing and electromagnetic separation. Zircon crystals were hand-picked under a binocular microscope. SHRIMP U–Pb analysis was conducted at the Beijing Ion Probe Center, Chinese Academy of Geological Sciences. Zircon crystals were mounted in epoxy resin together with the zircon standard (TEM) (417 Ma in age). Cathodoluminescence (CL) and optical microphotography techniques were used for examining zircon morphology, zoning characteristics, and interior structure (Fig. 6). The analytical procedure and data-processing methods are described in detail in Jian et al. (2003).

### 4.3. Rutile and apatite ID-TIMS U–Pb geochronology

Single crystals of hydrothermal rutile and apatite were selected from sample FJW-19. ID-TIMS U–Pb analysis was conducted at the

Isotope Geology Laboratory, Boise State University. The rutile and apatite grains were separated and transferred to 3-ml Teflon PFA beakers, sonicated, and rinsed twice with ultrapure H_2O. Samples were loaded into 300-μl Teflon PFA microcapsules with a weighed aliquot mixed $^{233}U-^{235}U-^{205}Pb$ tracer solution and 120 ml of 29 M HF with a trace of 3.5 M HNO_3 (rutile) or 1:1.6 M HCl:29 M HF (apatite). Microcapsules were placed in a large-capacity Parr vessel, and the crystals were dissolved at 220 °C for 48 h, dried to fluorides, and then redissolved in 6 M HCl at 180 °C overnight. U and Pb were separated from the dissolved matrix using a two-stage HBr- and HCl-based anion-exchange chromatographic procedure (Krogh, 1973) to purify Pb and U, respectively. Purified Pb and U were collected separately and dried with 2 μl of 0.05 N H_3PO_4.

Pb and U were loaded separately on outgassed zone-refined Re center filaments in 2 μl of a silica–gel/phosphoric acid mixture (Gerstenberger and Haase, 1997). Isotopic measurements were made on a GV Isoprobe-T multicollector thermal ionization mass spectrometer equipped with nine Faraday cups and an ion-counting Daly detector. Pb isotopes were measured by peak-jumping all isotopes on the Daly detector for 100–150 cycles and were corrected for (0.22 ± 0.04)%/a.m.u. mass fractionation. Transitory isobaric interference from high-molecular-weight organics, particularly on ^{204}Pb and ^{207}Pb, disappeared within approximately
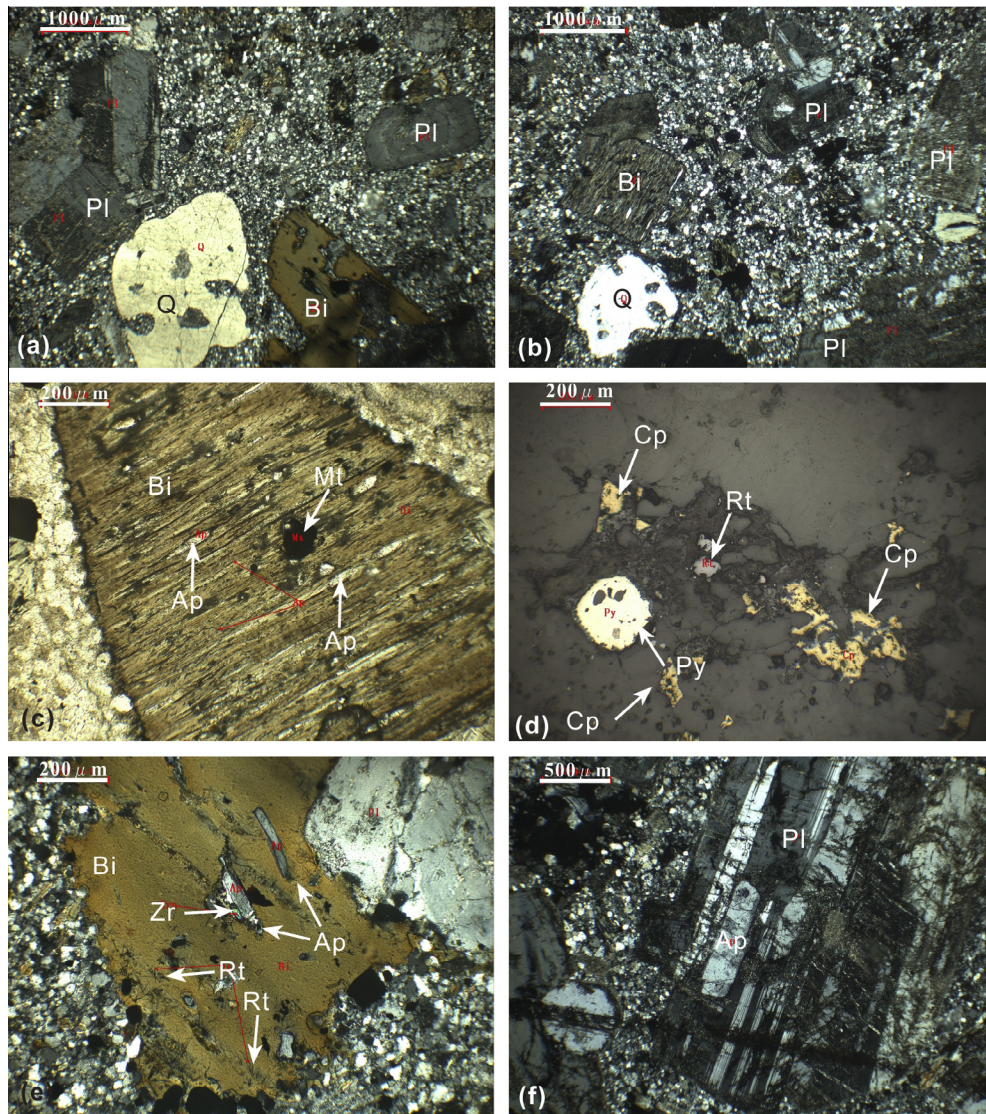
Fig. 5. Photomicrographs of sample FJW-19 and sample FJW-20. (a) Sample FJW-19 showing only minor hydrothermal alteration. (b) Sample FJW-20 showing only minor hydrothermal alteration. (c) Biotite phenocrysts exsolving apatite and magnetite along the cleavages. (d) Pyrite, chalcopyrite, rutile and quartz vein in sample FJW-19, demonstrating that the rutile precipitated with chalcopyrite mineralization. (e) Biotite phenocrysts exsolving apatite and rutile along the cleavages and a zircon inclusion in biotite. (f) Plagioclase phenocrysts with apatite inclusions. *Abbreviation*: bt = biotite, qz = quartz, cp = chalcopyrite, mt = magnetite, ht = hematite, pl = plagioclase, ap = apatite, rt = rutile.
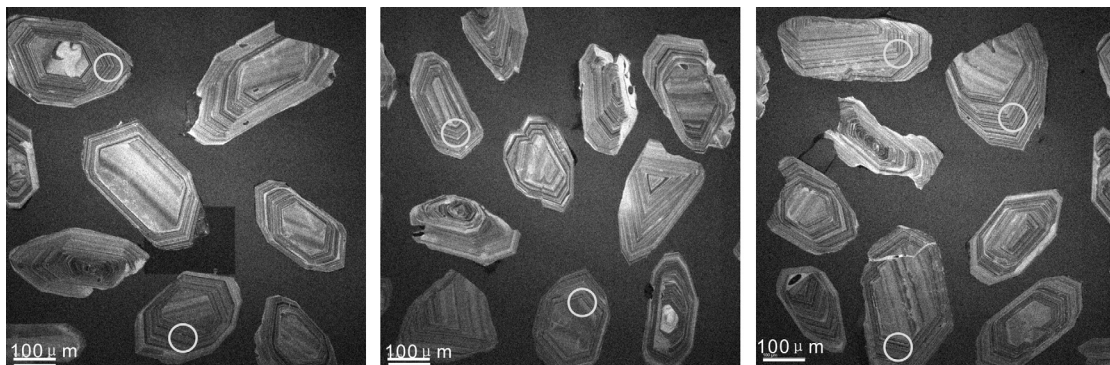
Fig. 6. Cathodoluminescent images of zircon from sample FJW-19. SHRIMP U–Pb analytical areas are indicated by circles and are approximately 25 μm in diameter. Cathodoluminescent images were acquired at the Institute of Mineral Resources, Chinese Academy of Geological Sciences, using a JOEL JXA 8800R, at 20 kV, 10 nA.

Table 1
Zircon SHRIMP U–Pb (FJW-19) analytical results of the granodiorite porphyry at Fujiawu Cu–Mo deposit, South China.

Spot	$^{206}Pbc\%$	U (ppm)	Th (ppm)	$^{232}Th/^{238}U$	$^{206}Pb^*$ (ppm)	$^{206}Pb/^{238}U$ age (Ma)	$^{207}Pb^*/^{206}Pb^*$	±%	$^{207}Pb^*/^{235}U$	±%	$^{206}Pb^*/^{238}U$	±%
Fjw-19-1.1	0.84	496	229	0.48	11.5	170.8 ± 3.2	0.0452	7.6	0.1670	7.9	0.02685	1.9
Fjw-19-2	1.17	566	318	0.58	13.2	170.4 ± 3.2	0.0401	7.7	0.1480	7.9	0.02679	1.9
Fjw-19-1.2	0.87	655	299	0.47	15.2	170.9 ± 3.1	0.0446	4.8	0.1650	5.2	0.02686	1.8
Fjw-19-3	0.24	734	359	0.51	17.8	179.2 ± 3.2	0.0487	3.3	0.1893	3.8	0.02819	1.8
Fjw-19-4	0.47	748	353	0.49	17.0	167.1 ± 3.0	0.0453	3.6	0.1642	4.0	0.02627	1.8
Fjw-19-5	1.14	430	168	0.40	9.57	163.1 ± 3.1	0.0443	8.0	0.1560	8.2	0.02562	1.9
Fjw-19-6	0.53	636	284	0.46	14.8	170.9 ± 3.1	0.0473	4.3	0.1751	4.7	0.02686	1.8
Fjw-19-7	0.68	359	149	0.43	8.49	173.9 ± 3.3	0.0452	8.4	0.1700	9.7	0.02735	1.9
Fjw-19-8	0.97	663	302	0.47	15.5	170.9 ± 3.1	0.0423	2.8	0.1565	3.3	0.02686	1.8
Fjw-19-9	1.15	566	253	0.46	13.0	168.1 ± 3.1	0.0417	3.8	0.1517	4.2	0.02640	1.8
Fjw-19-10	0.53	874	454	0.54	20.4	171.7 ± 3.1	0.0459	3.8	0.1710	4.2	0.02700	1.8
Fjw-19-11	0.47	584	290	0.51	13.7	172.7 ± 3.1	0.0472	3.9	0.1766	4.4	0.02716	1.8
Fjw-19-12	0.58	661	287	0.45	15.0	167.0 ± 3.1	0.0448	5.3	0.1621	5.6	0.02624	1.9
Fjw-19-13	1.09	439	180	0.42	9.91	165.3 ± 3.8	0.0445	7.2	0.1590	7.6	0.02597	2.3
Fjw-19-14	0.81	496	193	0.40	11.4	168.8 ± 3.2	0.0431	5.2	0.1578	5.6	0.02652	1.9
Fjw-19-15	0.67	563	265	0.49	13.5	176.1 ± 3.2	0.0467	4.7	0.1784	5.0	0.02770	1.8
Fjw-19-16	0.52	452	150	0.34	10.9	177.9 ± 3.3	0.0454	4.3	0.1750	4.7	0.02798	1.9

Errors are 1-sigma; Pbc and Pb* indicate the common and radiogenic portions, respectively.
Error in standard calibration was 0.87% (not included in above errors but required when comparing data from different mounts).
(1) Common Pb corrected using measured ^{204}Pb.
(2) Common Pb corrected by assuming $^{206}Pb/^{238}U$–$^{207}Pb/^{235}U$ age-concordance.
(3) Common Pb corrected by assuming $^{206}Pb/^{238}U$–$^{208}Pb/^{232}Th$ age-concordance.

30 cycles, while ionization efficiency averaged >10^4 cps/pg of each Pb isotope. Linearity (to ⩾1.4×10^6 cps) and the associated dead-time correction of the Daly detector were monitored by repeated analyses of NBS982, and have been constant since installation. Uranium was analyzed as UO_2^+ ions in static mode on three Faraday cups fitted with 10^{11} ohm resistors for 150–200 cycles and was corrected for isobaric interference of $^{233}U^{18}O^{16}O$ on $^{235}U^{16}O^{16}O$ with an $^{18}O/^{16}O$ ratio of 0.00206. Ionization efficiency averaged >30 mV/ng of each U isotope. U mass fractionation was corrected by using the known $^{233}U/^{235}U$ ratio of the tracer solution.

U–Pb isotope ratios, dates, and uncertainties for each analysis were calculated using the algorithms of Schmitz and Schoene (2007) and the U decay constants of Jaffey et al. (1971). Uncertainties are based upon nonsystematic analytical errors, including counting statistics, instrumental fractionation, tracer subtraction, and blank subtraction. Up to 0.5 pg of common Pb in the analyses was attributed to the laboratory blank and was subtracted based on the measured laboratory Pb isotopic composition and associated dispersion; U blanks are <0.1 pg. Sample isotope ratios and isochron calculations (for apatite) utilized these blank-, tracer-, and fractionation-corrected ratios. For the calculation of radiogenic isotope ratios and ages (for rutile), excess common Pb (over the blank amount) was subtracted by using the initial Pb isotopic composition (with uncertainties) defined by the apatite $^{238}U/^{204}Pb$–$^{206}Pb/^{204}Pb$ and $^{235}U/^{204}Pb$–$^{207}Pb/^{204}Pb$ isochrons. Radiogenic $^{206}Pb/^{238}U$ ratios and dates were also corrected for initial ^{230}Th disequilibrium using a Th/U$_{[fluid]}$ ratio of 3.

Nonsystematic errors on the sample isotope ratios and dates are reported as internal 2σ errors. These error estimates should be considered when comparing our isochron and $^{206}Pb/^{238}U$ dates with those from other laboratories in which tracer solutions calibrated against the EARTHTIME gravimetric standards were used. When comparing our dates with those derived from other decay schemes (e.g., $^{40}Ar/^{39}Ar$ or ^{187}Re–^{187}Os), the uncertainties in tracer calibration and ^{238}U decay constant (Jaffey et al., 1971) should be added to the internal error in quadrature. This total systematic error is ±0.2 Ma for the crystallization ages of the samples reported herein.

4.4. Biotite Ar–Ar geochronology

Biotite samples from FJW-19 and FJW-20 were purified using a magnetic separator and then cleaned in an ultrasonic ethanol bath. The purity of the analyzed grains (0.08–0.15 mm) was >99%. Sam-

Table 2
Zircon SHRIMP U–Pb (FJW-8) analytical results of the quartz diorite porphyry at Fujiawu Cu–Mo deposit, South China.

Spot	$^{206}Pbc\%$	U (ppm)	Th (ppm)	$^{232}Th/^{238}U$	$^{206}Pb^*$ (ppm)	$^{206}Pb/^{238}U$ age (Ma)	$^{207}Pb^*/^{206}Pb^*$	±%	$^{207}Pb^*/^{235}U$	±%	$^{206}Pb^*/^{238}U$	±%
FJW-8-1.1	0.70	383	179	0.48	8.71	167.3 ± 2.5	0.0532	2.3	0.172	5.9	0.02629	1.5
FJW-8-2.1	0.77	612	479	0.81	13.9	166.5 ± 2.5	0.05152	1.5	0.164	6.3	0.02617	1.5
FJW-8-3.1	0.44	828	528	0.66	19.1	169.9 ± 2.5	0.05103	1.2	0.1750	3.4	0.02670	1.5
FJW-8-4.1	0.81	377	180	0.49	8.80	171.6 ± 2.7	0.05624	1.8	0.185	6.5	0.02698	1.6
FJW-8-4.2	0.80	696	435	0.65	16.3	172.4 ± 2.6	0.05089	1.4	0.1662	5.2	0.02710	1.5
FJW-8-5.1	0.51	489	312	0.66	11.1	167.6 ± 2.4	0.05134	1.5	0.1716	3.2	0.02634	1.5
FJW-8-6.1	0.57	399	184	0.48	9.32	171.8 ± 2.7	0.05326	1.8	0.181	6.3	0.02701	1.6
FJW-8-7.1	0.74	808	479	0.61	18.6	169.7 ± 2.4	0.05119	1.2	0.1664	4.0	0.02668	1.4
FJW-8.9.1	0.43	677	460	0.70	15.0	163.4 ± 2.4	0.05009	1.4	0.1649	4.1	0.02566	1.5
FJW-8-10.1	0.85	522	324	0.64	11.9	168.0 ± 2.5	0.05293	1.4	0.168	6.7	0.02640	1.5
FJW-8-11.1	0.82	447	288	0.67	10.4	171.7 ± 2.5	0.05127	1.6	0.1665	5.3	0.02699	1.5

Errors are 1-sigma; Pbc and Pb* indicate the common and radiogenic portions, respectively.
Error in Standard calibration was 0.87% (not included in above errors but required when comparing data from different mounts).
(1) Common Pb corrected using measured ^{204}Pb.
(2) Common Pb corrected by assuming $^{206}Pb/^{238}U$–$^{207}Pb/^{235}U$ age-concordance.
(3) Common Pb corrected by assuming $^{206}Pb/^{238}U$–$^{208}Pb/^{232}Th$ age-concordance.

ples were irradiated for 51 h in the nuclear reactor at the Chinese Institute of Atomic Energy in Beijing and subsequently cooled for approximately 100 days. An $^{40}Ar/^{36}Ar$ stepwise heating analysis was performed at the Institute of Geology, Chinese Academy of Geological Science, using an MM-1200B mass spectrometer. Measured isotopic ratios were corrected for mass discrimination, atmospheric Ar component, blanks, and irradiation-induced mass interference. The decay constant used was $\delta = 5.543 \times 10^{-10}$/year (Steiger and Jäger, 1977). All ^{37}Ar values were corrected for radiogenic decay (half-life = 35.1 days). Uncertainty in each apparent age is given at the 2σ level. The monitor used in this work is an internal standard: Fangshan biotite (ZBH-25), for which the age is 132.7 Ma and potassium content is 7.6%. The J values of these monitors are given in Table 3. The detailed analysis techniques are described in Chen et al. (2002).

5. Results

5.1. Zircon SHRIMP U–Pb results

A total of 17 spots on 16 zircon grains from K-feldspar-altered granodiorite porphyry (sample FJW-19) were analyzed (Table 1). Cathodoluminescent images of zircon show well-preserved primary oscillatory growth zones with a euhedral to subeuhedral prismatic shape, and with no evidence for inheritance (Fig. 6). The zircon grains contain 359–874 ppm U, 149–454 ppm Th, and 8.49–20.4 ppm ^{206}Pb. The weighted mean of the 17 analyses yields a $^{206}Pb/^{238}U$ age of 172.0 ± 2.1 Ma (2σ; $n = 17$ and MSWD = 1.4) (Fig. 7).

A total of 11 spots on 10 zircon grains from sericite-altered quartz diorite porphyry (sample FJW-8) were analyzed (Table 2). As in sample FJW-19, cathodoluminescent images of zircon show well-preserved primary oscillatory zones with a euhedral to subeuhedral prismatic shape, and with no evidence for inheritance. The zircon grains contain 383–828 ppm U, 179–528 ppm Th, and 8.49–20.4 ppm ^{206}Pb. The weighted mean of the 12 analyses yields a $^{206}Pb/^{238}U$ age of 168.5 ± 1.4 Ma (2σ; $n = 12$ and MSWD = 1.5) (Fig. 7).

5.2. Rutile and apatite ID-TIMS results

Hydrothermal apatite from the granodiorite porphyry (FJW-19) comprised large, turbid to translucent crystals and crystal fragments. Three individual apatite crystal fragments were analyzed. Each grain contained approximately 10 ppm U and several parts per million of mostly (>75%) common Pb, thus compromising the utility of radiogenic model Pb age calculations (Table 3). As an alternative, three-point $^{238}U/^{204}Pb-^{206}Pb/^{204}Pb$ (Fig. 8A) and $^{235}U/^{204}Pb-^{207}Pb/^{204}Pb$ (Fig. 8B) isochrons were calculated, yielding a statistically robust isochron age of 164.4 ± 0.9 Ma (2σ, MSWD = 2.0) and 170 ± 18 Ma (2σ, MSWD = 0.31) and initial isotope compositions of ($^{206}Pb/^{204}Pb$)$_i$ = 18.215 ± 0.019 and ($^{207}Pb/^{204}Pb$)$_i$ = 15.605 ± 0.022 (Table 3).

Three individual rutile grains from the same sample were also analyzed, and both contained extremely small amounts of radiogenic Pb, from 0.3 to 0.5 pg (Table 3). Nonetheless, accurate $^{206}Pb/^{238}U$ dates were calculated from two single crystals (r2 and r3) because of their similarly low common Pb contents. These two grains yielded $^{206}Pb/^{238}U$ dates of 165.0 ± 1.1 and 164.8 ± 1.6 Ma (Fig. 8C), in good agreement with the isochron age for the apatite from the same sample. The hydrothermal rutile U–Pb ages are significantly younger than that of the host granodiorite (~7 million years) and slightly younger (~3 million years) than the quartz diorite porphyry.
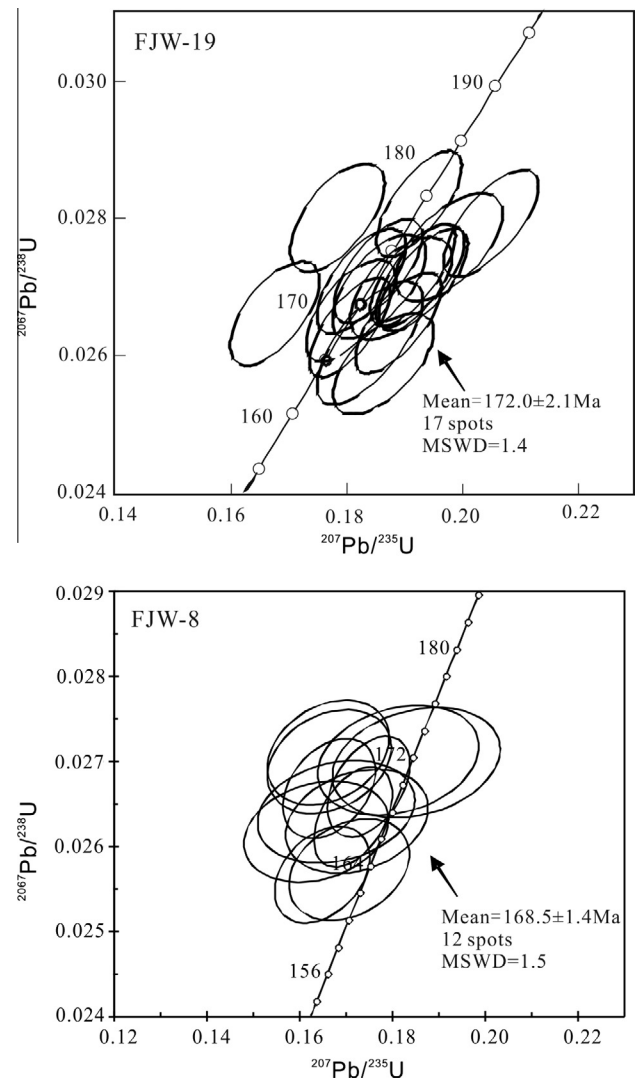

Fig. 7. Concordia plot showing all SHRIMP U–Pb data for zircons from sample FJW-19 and FJW-8.

5.3. Biotite Ar–Ar results

Argon–argon ages and 2σ uncertainties are plotted against the cumulative released ^{39}Ar fraction to establish the age spectra in Figs. 9 and 10. Argon isotope ratios are presented on correlation plots using the program ISOPLOT (Ludwig, 2003). The $^{40}Ar-^{39}Ar$ data are summarized in Table 4, which incorporates the apparent age spectra and the atmospheric argon and Ca:K ratios from each heating. Biotite from granodiorite sample FJW-19 has a plateau age of 169.9 ± 1.8 Ma, calculated from steps 9–13, representing 52.4% of the total argon release (Fig. 9a). The isochron age of 171.0 ± 3.0 Ma (MSWD = 2.2, initial $^{40}Ar/^{36}Ar$ = 228) is concordant with the plateau age (Fig. 9b). The total age for granodiorite sample FJW-19 is about 167.3 Ma.

The biotite from granodiorite sample FJW-20 sample has a plateau age of 168.7 ± 1.8 Ma, calculated from steps 9–13, representing 41.8% of the total argon release (Fig. 10a). The isochron age of 168.8 ± 6.1 Ma (MSWD = 2.5, initial $^{40}Ar/^{36}Ar$ = 321) is concordant with the plateau age within the error (Fig. 10b) and the total age is about 164.1 Ma.

Both samples show some Ar loss in the low-temperature step that may indicate minor Ar loss from grain margins. They also show a drop in apparent age in the highest temperature steps, which may indicate degassing of a secondary phase, probably chlorite.

Table 3
ID-TIMS U–Pb age data of rutile and apatite from sample FJW-19 at Fujiawu Cu–Mo deposit.

Sample (a)	Compositional parameters					Radiogenic isotopic ratios					Model ages			
	$^{206}Pb^* \times 10^{-13}$ mol (b)	$^{206}Pb^*$ (mol%) (b)	Pb*/Pbc (b)	Pbc(pg) (b)	$^{206}Pb/^{204}Pb$ (c)	$^{207}Pb/^{235}U$ (d)	% err (e)	$^{206}Pb/^{238}U$ (d)	% err (e)	corr.corf.	$^{207}Pb/^{235}U$ (f)	± (e)	$^{206}Pb/^{238}U$ (f)	± (e)
r1	0.0119	18.63	0.06	4.31	22.4	0.15464	130.9	0.025264	2.125	0.159	146.0	178.1	160.8	3.4
r2	0.0255	77.60	0.90	0.61	82.7	0.16242	22.3	0.025921	0.658	0.282	152.8	31.6	165.0	1.1
r3	0.0146	62.46	0.43	0.72	49.2	0.16258	49.4	0.025893	0.963	0.251	153.0	70.2	164.8	1.6
a1	0.2585	10.04	0.06	192.8	20.2									
a2	0.2680	24.44	0.14	69.0	24.1									
a3	0.2550	7.15	0.05	275.6	19.6									

(a) a, apatite; r, rutile; all analyses composed of single crystals or crystal fragments. (b) Pb* and Pbc represent radiogenic and common Pb, respectively; mol% $^{206}Pb^*$ with respect to radiogenic, blank and initial common Pb. (c) Measured ratio corrected for spike and fractionation only. Pb isotope ratios were corrected for instrumental mass fractionation of 0.18%/a.m.u., based on analysis of NBS-981 and NBS-982. (d) Corrected for fractionation, spike, and common Pb; up to 1 pg of common Pb was assumed to be procedural blank: $^{206}Pb/^{204}Pb$ = 18.60 ± 0.80%; $^{207}Pb/^{204}Pb$ = 15.69 ± 0.32%; $^{208}Pb/^{204}Pb$ = 38.51 ± 0.74% (all uncertainties 1-sigma). Excess over blank was assigned to initial common Pb. (e) Errors are 2-sigma, propagated using the algorithms of Schmitz and Schoene (2007). (f) Calculations are based on the decay constants of Jaffey et al. (1971). $^{206}Pb/^{238}U$ and $^{207}Pb/^{206}Pb$ ages corrected for initial disequilibrium in $^{230}Th/^{238}U$ using Th/U [magma] = 3.
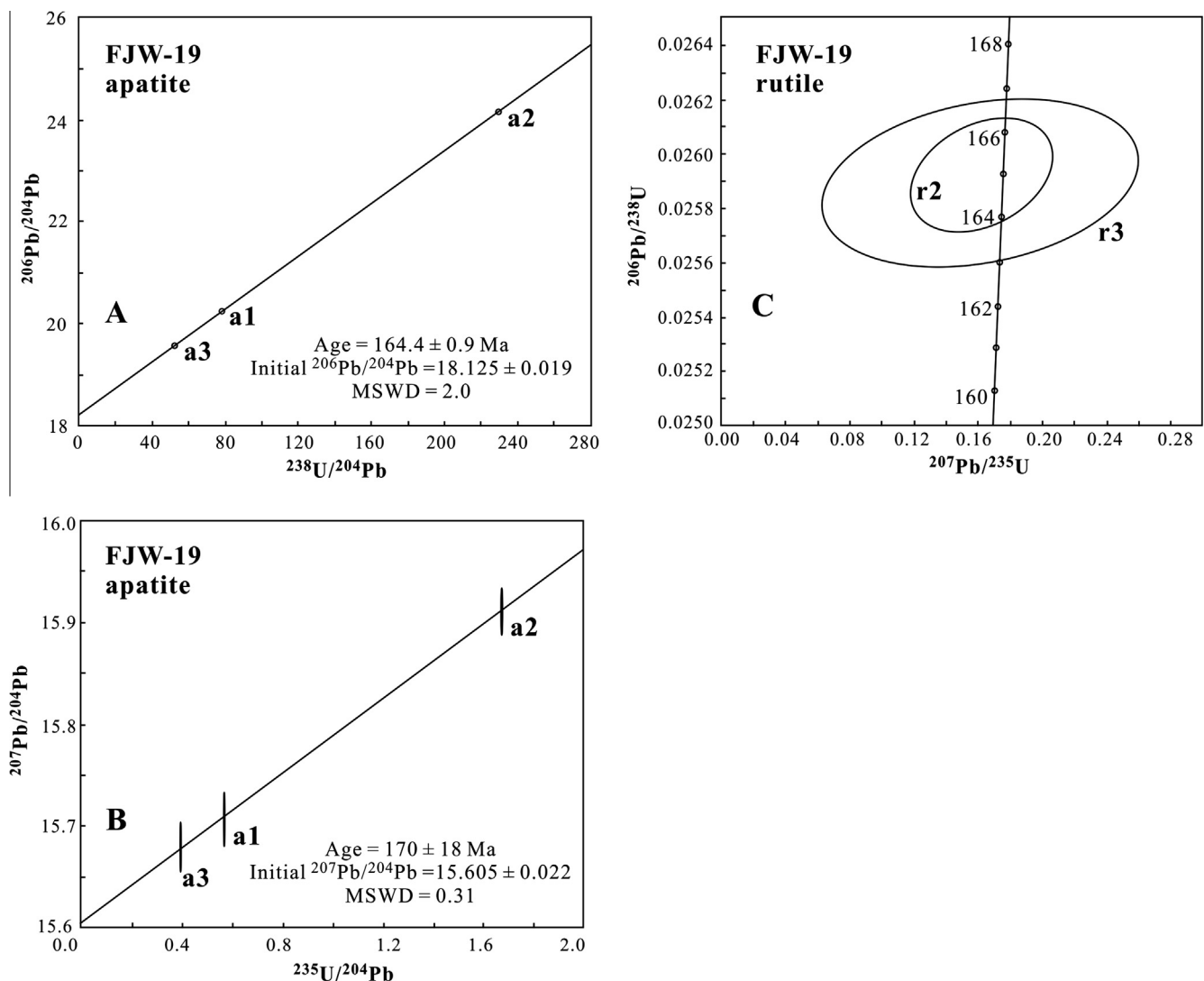
Fig. 8. Plot showing the ID-TIMS data of apatite and rutile from sample FJW-19. (A) apatite $^{238}U/^{204}Pb$–$^{206}Pb/^{204}Pb$ isochrons isochron age; (B) apatite $^{235}U/^{204}Pb$–$^{207}Pb/^{204}Pb$ isochron age; (C) rutile $^{207}Pb/^{235}U$–$^{206}Pb/^{238}U$ age.

6. Discussion

6.1. Previous dating studies in the Fujiawu deposit and adjacent areas

Previous studies on the Dexing porphyry Cu–Mo deposits focus mostly on the Tongchang porphyry Cu–Mo deposit. The available

Rb–Sr and K–Ar ages of the porphyries fall in a wide range from 193 to 112 Ma (Early Jurassic–Cretaceous) and are unreliable because of extensive hydrothermal alteration (Zhu et al., 1983; Rui et al., 1984; Huang et al., 2001; Table 5, Fig. 11).

Previous K–Ar dating of vein-hosted hydrothermal K-feldspar in granodiorite and phyllite gave results of 157 and 152 Ma,

respectively (Zhu et al., 1983). K–Ar whole rock dates of granodiorite porphyry are 163 Ma (Zhu et al., 1983). Sericite in phyllitic alteration yielded K–Ar dates of ~112 Ma, and biotite from quartz diorite porphyry yielded K–Ar ages of ~100 Ma (Huang et al., 2001). All of the above extremely young dates, derived from K–Ar dating, are likely incorrect because there is no evidence for other magmatic or hydrothermal activity of similar timing in the region. Furthermore, more recent and robust ages of both porphyritic intrusives and related ores have been reported. A zircon SHRIMP U–Pb date of the granodiorite in the Fujiwau deposit (similar to samples FJW-19 and FJW-20) indicates magma emplacement at 171 ± 3 Ma (Wang et al., 2006). Recent molybdenite Re–Os isochron ages show that Mo mineralization at Fujiawa occurred very soon after or during magma emplacement at 170.9 ± 1.5 Ma (Guo et al., 2012).

6.2. Interpretation of U–Pb and Ar–Ar ages

Nearly all zircon crystals in the present study were euhedral grains, with bipyramidal terminations, or were fragments of such grains. Cathodoluminescent images show clear chemical zonation with no inherited cores. The Th/U ratios from granodiorite sample FJW-19 and quartz-diorite sample FJW-8 have narrow ranges from 0.34 to 0.58 and from 0.48 to 0.81, respectively, which is consistent with their igneous origin (cf. Hoskin and Schaltegger, 2003; Bacon and Lowenstern, 2005).

The zircon SHRIMP U–Pb age from sample FJW-19 represents the age of emplacement of the granodiorite porphyry, at 172.0 ± 2.1 Ma, which is consistent with the zircon SHRIMP U–Pb age of 171 ± 3 Ma reported previously by Wang et al. (2006). The zircon SHRIMP U–Pb age from sample FJW-8 indicates that the quartz-diorite porphyry was emplaced several million years later at 3–4 Ma and attests to multiple stages of magma emplacement at the Fujiawu deposit.
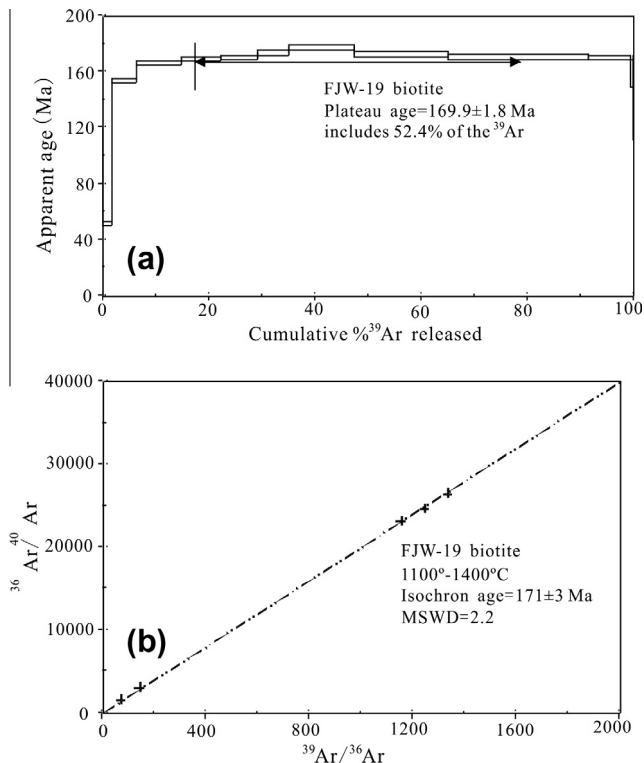

Fig. 9. (a) $^{40}Ar/^{39}Ar$ plateau ages, and (b) isochron age of biotite from sample FJW-19.
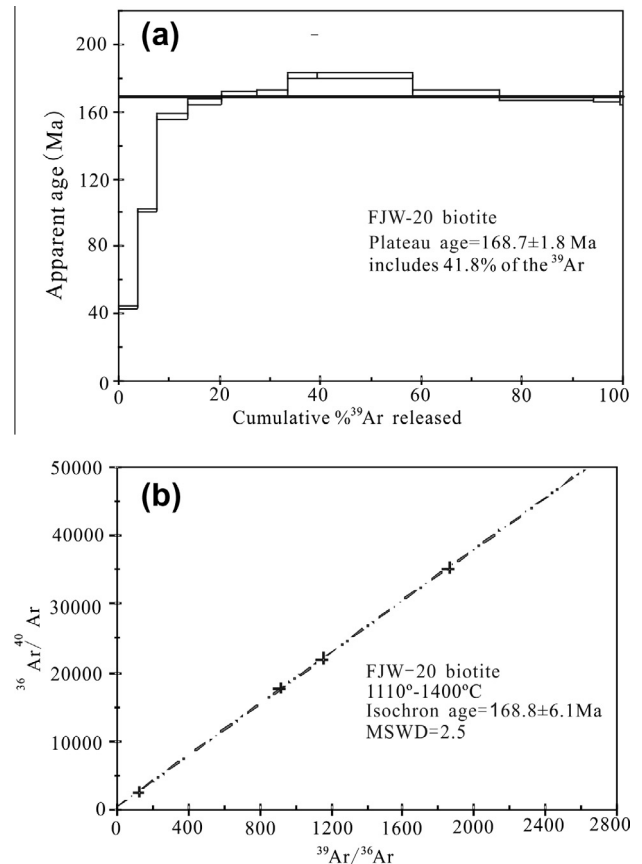

Fig. 10. (a) $^{40}Ar/^{39}Ar$ plateau ages, and (b) isochron age of biotite from sample FJW-20.

Hydrothermal apatite in the granodiorite yields an ID-TIMS U–Pb isochron age of 164.4 ± 0.9 Ma, and the two hydrothermal rutile grains yield model ages of 165.0 ± 1.1 and 164.8 ± 1.6 Ma. The concordance of the apatite U–Pb age and the rutile ages is interpreted as supporting their cocrystallization during hydrothermal alteration of the host porphyry. The age of this hydrothermal event is 3–4 million years younger than the age of quartz diorite emplacement and 6–7 million years after the emplacement of the host granodiorite. The integrated hydrothermal biotite ^{40}Ar–^{39}Ar ages of the granodiorite samples are interpreted as the timing of hydrothermal activity. The plateau ages of 169.9 ± 1.8 and 168.7 ± 1.8 Ma suggest that the hydrothermal system had cooled below 350 °C by about 169 Ma and that subsequent Cu mineralization several million years later might have disturbed the Ar–Ar in biotite isotopic system.

6.3. Magmatism, hydrothermal alteration, and mineralization

The duration of magmatism, hydrothermal activity, and cooling history may be key factors in controlling Cu–Mo mineralization in porphyry deposits. It is widely assumed that giant porphyry Cu–Mo deposits are the products of exceptionally protracted and/or unusually multistage histories of magmatism, alteration, and mineralization. Porphyry Cu–Mo lifespans determined using multiple chronometers are commonly longer than those determined based on a single geochronometer. This age disparity reflects the fact that Re–Os ages account for only molybdenite mineralization but may neglect later intrusive events and the duration of cooling. In contrast, biotite Ar–Ar ages typically reflect the age of potassic alteration (at 250–400 °C; Richard and Noble, 1998), thereby taking

Table 4
$^{40}Ar/^{36}Ar$ stepwise heating data of biotite in the granodiorite porphyry (FJW-19 and FJW-20).

| T (°C)	$^{40}Ar/^{39}Ar$	$^{36}Ar/^{39}Ar$	$^{37}Ar/^{39}Ar$	$^{38}Ar/^{39}Ar$	^{40}Ar (%)	$^{40}Ar^*/^{39}Ar$	^{39}Ar (×10^{-14} mol)	^{39}Ar (Cum.) (%)	Age (Ma)	±1σ (Ma)
Sample: FJW-19 biotite, W = 25.25 mg, J = 0.004976										
600	172.7327	0.5497	0.0000	0.1502	5.96	10.2891	0.02	0.08	90	29
700	24.6760	0.0640	0.0724	0.0364	23.38	5.7696	0.47	1.92	51.1	1.1
780	37.8850	0.0680	0.0198	0.0433	46.92	17.7761	1.15	6.47	152.9	1.5
830	21.3580	0.0071	0.0119	0.0347	90.14	19.2527	2.18	15.07	165.0	1.6
880	20.5200	0.0030	0.0063	0.0339	95.62	19.6211	1.88	22.48	168.1	1.6
930	20.4177	0.0022	0.0053	0.0346	96.73	19.7511	1.72	29.27	169.1	1.6
990	20.7086	0.0019	0.0055	0.0352	97.29	20.1484	1.49	35.14	172.4	1.7
1050	21.1154	0.0015	0.0108	0.0359	97.87	20.6651	3.16	47.63	176.6	1.7
1100	20.3096	0.0009	0.0080	0.0351	98.67	20.0405	4.48	65.33	171.5	1.6
1150	20.0344	0.0008	0.0071	0.0350	98.84	19.8012	6.67	91.66	169.5	1.6
1200	20.0160	0.0008	0.0198	0.0360	98.75	19.7664	2.03	99.67	169.2	1.6
1260	21.6746	0.0110	0.0000	0.0363	84.98	18.4195	0.07	99.94	158.2	9.8
1400	36.0428	0.0668	0.3112	0.0424	45.32	16.3373	0.02	100.00	141	30
Sample: FJW-20 biotite, W = 25.85 mg, J = 0.005225										
700	69.0900	0.2178	0.1695	0.0727	6.84	4.7278	0.85	3.79	44.02	0.92
750	41.5314	0.1031	0.0613	0.0520	26.61	11.0517	0.82	7.44	101.3	1.1
800	24.0480	0.0224	0.0159	0.0448	72.44	17.4208	1.35	13.47	157.2	1.6
850	19.9838	0.0054	0.0190	0.0430	92.04	18.3927	1.52	20.28	165.5	1.6
900	20.7576	0.0064	0.0273	0.0437	90.93	18.8757	1.55	27.22	169.7	1.7
950	20.6191	0.0053	0.0230	0.0438	92.36	19.0440	1.37	33.34	171.1	1.7
1000	21.8084	0.0053	0.0403	0.0468	92.83	20.2454	1.30	39.16	181.4	1.8
1070	20.8263	0.0019	0.0370	0.0461	97.33	20.2704	4.27	58.22	181.6	1.7
1110	19.3144	0.0011	0.0243	0.0439	98.32	18.9900	3.85	75.43	170.7	1.6
1150	18.8331	0.0005	0.0153	0.0434	99.13	18.6700	4.21	94.24	167.9	1.6
1200	18.8673	0.0009	0.0092	0.0435	98.63	18.6081	1.15	99.39	167.4	1.7
1400	21.0675	0.0081	0.0080	0.0439	88.68	18.6825	0.14	100.00	168.0	3.9

Table 5
Summary of radiometric age data of the igneous rocks and related hydrothermal alteration and mineralization in Dexing porphyry Cu–Mo district, South China.

Deposits	Host rocks	Analyzed rocks/minerals	Methods	Age (Ma)	References
Fujiawu	Quartz-K-feldspar vein in granodiorite	K-feldspar	K–Ar	157	Huang et al. (2001)
Fujiawu	Quartz-K-feldspar vein in phyllite	K-feldspar	K–Ar	152	Huang et al. (2001)
Fujiawu	Phyllic alteration zone	Sericite	K–Ar	112	Huang et al. (2001)
Fujiawu	Granodiorite	Whole rock	K–Ar	163	Huang et al. (2001)
Fujiawu	Quartz diorite porphyry	Biotite	K–Ar	100	Huang et al. (2001)
Tongchang	Granodiorite porphyry	Zircon	SHRIMP U–Pb	171 ± 3	Wang et al. (2006)
Fujiawu	Granodiorite porphyry	Zircon	SHRIMP U–Pb	171 ± 3	Wang et al. (2006)
Tongchang	Molyndenite vein	Molybdenite	Re–Os	170.4 ± 1.8	Lu et al. (2005)
Fujiawu	Molyndenite vein	Molybdenite	Re–Os	170.9 ± 1.5	Guo et al. (2012)
Fujiawu	Granidiorite porphyry	Zircon	SHRIMP U–Pb	172.0 ± 2.1	This study
Fujiawu	Quartz diorite porphyry	Zircon	SHRIMP U–Pb	168.5 ± 1.4	This study
Fujiawu	Granidiorite porphyry	Rutile	ID-TIMS U–Pb	165.0 ± 1.1	This study
				164.8 ± 1.6	
Fujiawu	Granidiorite porphyry	Apatite	ID-TIMS U–Pb	164.4 ± 0.9	This study
Fujiawu	Granidiorite porphyry	Biotite	Ar–Ar	169.9 ± 1.8	This study
Fujiawu	Granidiorite porphyry	Biotite	Ar–Ar	168.7 ± 1.8	This study

no account of the early magmatism events (at 400 °C to >800 °C) during which porphyry intrusion occurs. However, Re–Os molybdenite dating of some porphyry Cu deposits also suggests protracted, albeit probably minimum, lifespans similar to those determined by the U–Pb methods (Barra et al., 2005). Therefore, intergrative geochronology of ore deposits might provide insight into the duration and timing of hydrothermal circulation, as well as the cooling history for the formation of the porphyry Cu–Mo deposit. Recent studies show that some large porphyry-type ore deposits are the result of the superposition of multiple ore-forming events (cf. Rusk et al., 2006, 2008; Sillitoe, 2010). The ore-forming may postdate emplacement of the host pluton by tens of millions of years. Several major central Andean porphyry Cu systems were intermittently magmatically and hydrothermally active for at least 3–5 Ma (e.g., Quellaveco: 4.07 ± 0.82 Ma, Sillitoe and Mortensen, 2010; Antapaccay: 5.2 ± 0.7 Ma, Jones et al., 2007; Escondida: 4.2 ± 1.0 Ma, Padilla-Garza et al., 2004; Chuquicamata: 3.5 ± 0.4 Ma, Ballard et al., 2001; Elatsite: 0.7 ± 0.3 Ma, von Quadt et al., 2002; and La Caridad: 0.7 ± 0.3 Ma, Valencia et al., 2005).

A number of K–Ar ages ranging from 165 to 100 Ma (Zhu et al., 1983) have been reported for alteration and clay minerals for the Dexing porphyry Cu–Mo district including the Fujiawu deposit and are thought to represent mineralization ages. However, the range in ages strongly suggests that the K–Ar system has been significantly disturbed and/or represents a mixture of materials that predate mineralization. We therefore conclude that K–Ar ages have no geological meaning in the context of the Dexing porphyry Cu–Mo deposit.

Our zircon SHRIMP U–Pb age (172.0 ± 2.1 Ma) is similar to that (171 ± 3 Ma) of Wang et al. (2006) and suggests that the granodiorite magma was emplaced at 172 Ma. Lu et al. (2005) reported a molybdenite Re–Os age of 171 Ma at the Tongchang porphyry Cu–Mo deposit, and Guo et al. (2012) reported a molybdenite Re–Os age of 170.9 ± 1.5 Ma at the Fujiawu porphyry Cu–Mo deposit. These data indicate that molybdenum mineralization closely followed the granodiorite intrusion emplacement. The Mo mineralization at Fujiawu is synchronous with that at Tongchang. Zircon U–Pb closure temperatures are estimated to be ~800 °C (Hodges,
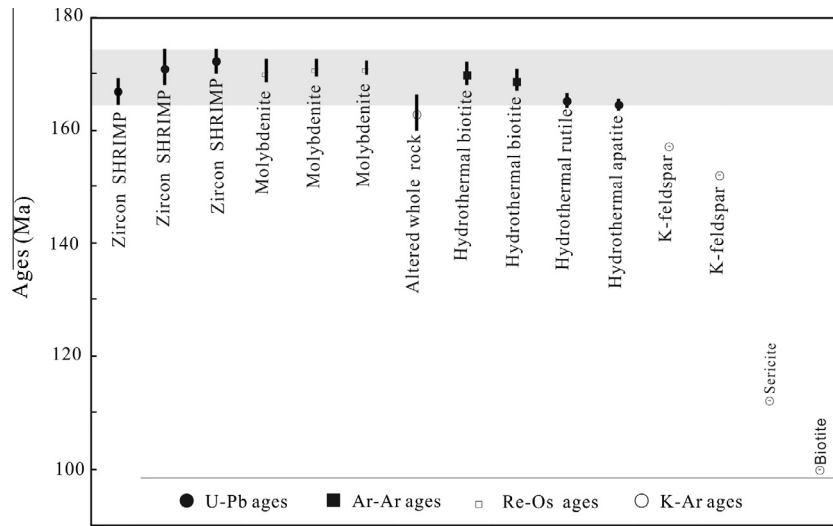
Fig. 11. Geochronology of the Dexing porphyryCu–Mo district, Southeast China. Limits on the age of emplacement for igneous intrusions at Dexing are shown in shaded gray area.

1991), and the Mo precipitated at ~450 °C at the Dexing Cu–Mo deposit (Zhu et al., 1983). These results indicate a relatively rapid cooling history [350 °C/(10^6 years)] subsequent to magma emplacement during molybdenite mineralization.

The association of rutile with chalcopyrite in hydrothermal quartz veins suggests that the rutile age may reflect the age of copper mineralization (Fig. 5D). Rutile has been used in numerous instances for dating hydrothermal events (Richards et al., 1988; Wong et al., 1989; Jemielita et al., 1989; Corfu and Muiir, 1989; Peytcheva et al., 2004; Kouzmanov et al., 2009), but its closure temperature is not well constrained (Schandl et al., 1990). Mezger et al. (1989) suggested a closure temperature of ~400 °C based on the assumption that the rutile ages record a thermal closure temperature rather than a hydrothermal crystallization event during the waning stages of metamorphism in high-grade terranes. Thus rutile precipitated at lower temperatures during hydrothermal activity reflects the hydrothermal rutile crystallization age (Schandl et al., 1990). We infer that the D veins that host the rutile and the majority of the copper in the Fujiawa deposit precipitated at temperatures (~200–300 °C; Zhu et al., 1983) at or below 300 °C (below the closure temperature of Ar–Ar in biotite). The apatite U–Pb age is similar to the age of rutile U–Pb and suggests they formed simultaneously. The rutile U–Pb age and apatite U–Pb age and the association between the rutile and chalcopyrite in quartz vein indicate that the chalcopyrite precipitated at 165 Ma after the emplacement of quartz diorite porphyry (168.5 ± 1.4 Ma) and after Mo mineralization in B veins. The rutile, apatite U–Pb, and zircon U–Pb ages indicate the slow cooling hydrothermal history after the quartz diorite emplacement. Thus cooling from the time of magma emplacement to the time of copper mineralization was relatively slow [occurring at a rate of 100–200 °C/(10^6 years)], taking approximately 4 million years. The span of the entire magmatic hydrothermal system in the Fujiawu deposit was closer to 6–7 million years, which is similar to the time span of the magmatic hydrothermal system that formed the Chuquicamata district, Chile (Barra, 2012).

7. Conclusions

Granodiorite porphyry and quartz diorite porphyry zircons yield a weighted mean ^{206}Pb/^{238}U age of 172.0 ± 2.1 and 168.5 ± 1.4 Ma in the Fujiawu porphyry Cu–Mo deposit of the Dex-

ing district, China. Two hydrothermal biotites give Ar–Ar step-heating plateau ages of 169.9 ± 1.8 and 168.7 ± 1.8 Ma, respectively. Apatite yielded an ID-TIMS isochron age of 164.4 ± 0.9 Ma, which is similar to ages from rutile (165.0 ± 1.1 and 164.8 ± 1.6 Ma). These ages indicate that the magmatism, hydrothermal activity, and Cu–Mo mineralization of the Fujiawu porphyry Cu–Mo deposit occurred in the Middle Jurassic. The Mo mineralization closely followed the granodiorite magma emplacement, whereas the Cu mineralization followed quartz diorite porphyry emplacement several million years later. Taken together, the geochronologic data suggest that Mo precipitation immediately followed magma emplacement, whereas Cu mineralization occurred after the hydrothermal system slowly cooled over several million years.

References

Bacon, C.R., Lowenstern, J.B., 2005. Late Pleistocene granodiorite source for recycled zircon and phenocrysts in rhyodacite lava at Crater Lake Oregon. Earth and Planetary Sciences Letter 233, 277–293.

Ballard, J.R., Palin, J.M., Williams, I.S., Campbell, I.H., Faunes, A., 2001. Two ages of porphyry intrusion resolved for the super-giant Chuquicamata copper deposit of northern Chile by ELA-ICP-MS and SHRIMP. Geology 29, 383–386.

Barra, F., 2012. Lifetimes of Chilean porphyry copper deposits. SEG 2012 Conference Abstract: Integrated Exploration and Ore Deposits.

Barra, F., Ruiz, J., Valencia, V.A., Ochoa-landin, L., Chesley, J.T., Zurcher, L., 2005. Laramide porphyry Cu–Mo mineralization in Northern Mexico: age constrains from Re–Os geochronology in molybdenite. Economic Geology 100, 1605–1616.

Charvet, J., Shu, L.S., Shi, Y.S., Guo, L.Z., Faure, M., 1996. The building of South China: collision of Yangtze and Cathaysia blocks, problems and tentative answers. Journal of Southeast Asian Earth Sciences 13, 223–225.

Chen, W., Zhang, Y., Ji, Q., Wang, S.S., Zhang, J.X., 2002. The magmatism and deformation times of the Xidaatan rock series, East Kunlun Mountain. Science in China (Series B) 45, 20–27.

Corfu, F., Muiir, T.L., 1989. The Hemlo-Heron Bay greenstone belt and Hemlo Au–Mo deposit, Superior Province, Ontario, Canada. 2. Timing of metamorphism, alteration and Au mineralization from titanite, rutile and monazite U–Pb geochronology. Chemical Geology (Isotope Geoscience Section) 79, 201–223.

Gerstenberger, H., Haase, G., 1997. A highly effective emitter substance for mass spectrometric Pb isotope ratio determinations. Chemical Geology 136, 309–312.

Guo, L.Z., Shi, Y.S., Ma, R.S., 1980. The geotectonic framework and crustal evolution of South China. In: Scientific papers on geology for international exchange, 1. Geological Publishing House, Beijing, pp 109–116 (in Chinese with English abstract).

Guo, S., Zhao, Y.Y., Qu, H.C., Wu, D.X., Xu, H.L., Li, C., Liu, Y., Zhu, X.Y., Wang, Z.K., 2012. Geological characteristics and ore-forming time of the Dexing porphyry copper ore mine in Jiangxi Province. Acta Geologica Sinica 86, 691–699.

Gustafson, L.B., Hunt, J.P., 1975. The porphyry copper deposit at El Salvador, Chile. Economic Geology 70, 857–912.

Hodges, K., 1991. Pressure–temperature–time paths: annual review of earth and planetary. Science 19, 207–236.

Hoskin, P.W.O., Schaltegger, U., 2003. The composition of zircon and igneous and metamorphic petrogenesis. Reviews in Mineralogy and Geochemistry 53, 2–62.

Hu, S.X., Chen, W., Hua, R.M., 1992. Lateral zoning of pneumatolytic-hydrothermal deposit mechanism of its formation. Mineral Deposit 11, 291–300 (in Chinese with English abstract).

Hua, R.M., Li, X.F., Lu, J.J., Chen, P.R., Qiu, D.T., Wang, G., 2000. Study on the tectonic setting and ore-forming fluid of Dexing large ore-concentrating area, Northeast Jiangxi Province. Advance in Earth Science 15, 525–533 (in Chinese with English abstract).

Huang, C.K., Bai, Y., Zhu, Y.S., Wang, H.Z., Shang, X.Z., 2001. Chinese copper deposits. Geological Publishing House, Beijing, p705.

Jaffey, A.H., Flynn, K.F., Glendenin, L.E., Bentley, W.C., Essling, A.M., 1971. Precision measurements of half-lives and specific activities of ^{235}U and ^{238}U. Physical Review C 4, 1889–1906.

Jemielita, R.A., Davis, D.W., Krogh, T.E., Spooner, E.T.C., 1989. Chronological constrsints on the origin of Archean lode gold deposits in the southern Supeior Province from U–Pb isotopic analysis of hydrothermal rutile and titanite. Geological Society of American Abstracts with Programs 21 (6), A351.

Jian, P., Liu, D.Y., Sun, X.M., 2003. SHRIMP dating of Carboniferous Jinshajiang ophiolite in western Yunnan and Sichuan: geochronological constraints on the evolution of the paleo-Tethys oceanic crust. Acta Geological Sinica 77, 217–277 (in Chinese with English abstract).

Jones, B., Kamenetsky, V., Davidson, P., and Allen, C., 2007. Antapaccay porphyry Cu–Au deposit: a product of Andean tectonism and evolving magmatism, late Eocene-early Oligocene Abancay batholith, Altiplano, southern Peru [abs.]: Ores and orogenesis. A symposium honoring the career of William R. Dickinson, Tucson, 2007, Program with Abstracts: Tucson, Arizona Geological Society, pp. 132–133.

Kouzmanov, K., Moritz, R., Quad, Av., Chiaradia, M., Peytcheva, I., Fontignie, D., Ramboz, C., Bogdanov, K., 2009. Late Cretaceous porphyry Cu and epithermal Cu–Au association in the Southern Panagyurishte District, Bulgaria: the paired Vlaykov Vruh and Elshitsa deposits. Mineralium Deposita 44, pp. 611–646.

Krogh, T.E., 1973. A low contamination method for hydrothermal decomposition of zircon and extraction of U and Pb for isotopic age determination. Geochimica et Cosmochimica Acta 37, 485–494.

Li, X.F., Sasaki, M., 2007. The hydrothermal alteration and mineralization of Middle Jurassic Dexing porphyry Cu–Mo deposit, Southeast China. Resource Geology 57 (4), 409–426.

Li, X.F., Watanabe, Y., Hua, R.M., Mao, J.W., 2008. Mesozoic Cu–Mo–W–Sn mineralization and ridge/triple subduction in South China. Acta Geologica Sinica 82, 625–640 (in Chinese with English abstract).

Li, X.F., Wang, C.Z., Hua, R.M., Wei, X.L., 2010. Fluid origin and structural enhancement during progressively localized mineralization of the Jinshan orogenic gold deposit, south China. Mineralium Deposita 45, 583–597.

Li, X.F., Feng, Z.H., Xiao, R., Song, C.A., Yang, F., Wang, C.Y., Mao, W., 2012. The typical metallic deposits, geochronological and tectonic seeting in Northeast Guangxi Province, South China. Acta Geological Sinica 86, 1713–1725.

Lu, J.J., Hua, R.M., Yao, C.L., 2005. Re–Os age for molybdenite from the Dexing porphyry Cu–Au deposit of Jiangxi province, China. Geochim Cosmochim Acta 69 (Suppl. A), 882.

Ludwig, K.R., 2003. User's Manual for Isoplot 3.00. Berkeley Geochronology Center, Berkeley, CA, 70 p.

Mezger, K., Hanson, G.N., Bohlen, S.R., 1989. High precision U–Pb ages of metamorphic rutile: application to the cooling history of high-grade terrains (abs.). EOS 70, 485–486.

Padilla-Garza, R.A., Titley, S.R., Eastoe, C.J., 2004. Hypogene evolution of the Escondida porphyry copper deposit. vol. 11. Society of Economic Geologists Special Publication, Chile, pp. 141–165.

Peytcheva, I., von Quadt, A., Ovtcharova, M., Handler, R., Neubauer, F., Salnikova, E., Kostitsyn, Y., Sarov, S., Kolcheva, K., 2004. Metagranitoids from the eastern part of the Central Rhodopean Dome (Bulgaria): U–Pb, Rb–Sr and 40Ar/39Ar timing of emplacement and exhumation and isotope-geochemical features. Mineralogy and Petrology 82, 1–31.

Richard, J.P., Noble, S.R., 1998. Application of radiogenic isotope systems to the timing and origin of hydrothermal systems. Reviews in Economic Geology 10, 195–233.

Richards, J.P., Krogh, T.E., Spooner, E.T., 1988. Fluids inclusion characteristics and U–Pb rutile age of late hydrothermal alteration and veining at the Musoshi stratiform copper deposit, Central African copper belt, Zaire. Economic Geology 83, 118–139.

Rui, Z.Y., Huang, C.K., Qi, G.M., 1984. Porphyry copper (molybdenite) deposits of China. Geological Publishing House, Beijing, p305.

Rui, Z.Y., Zhang, L.S., Wu, C.Y., Wang, L.S., Sun, X.Y., 2005. Dexing porphyry copper deposits in Jiangxi, China. In: Porter, T.M. (Ed.), Super porphyry copper and gold deposits: A global perspective, vol. 2. PGC Publishing, Adelaide, pp. 409–421.

Rusk, B., Reed, M., Dilles, J., Kent, A., 2006. Intensity of quartz cathodoluminescence and trace element content of quartz from the porphyry copper deposit in Butte, Montana. American Mineralogist 91, 1300–1312.

Rusk, B., Reed, M., Dilles, J.H., 2008. Fluid inclusion evidence for magmatic-hydrothermal fluid evolution in the porphyry copper-molybdenum deposit, Butte, Montana. Economic Geology 103, 307–334.

Schandl, E.S., Davis, D.W., Krogh, T.E., 1990. Are the alteration halos of massive sulfide deposits syngenetic: evidence from U–Pb dating of hydrothermal rutile at the Kidd volcanic center, Abitibi subprovince, Canada. Geology 18, 505–508.

Schmitz, M.D., Schoene, B., 2007. Derivation of isotope ratios, errors and error correlations for U–Pb geochronology using 205Pb–235U–(233U)-spiked isotope dilution thermal ionization mass spectrometric data. Geochemistry, Geophysics, Geosystems (G3) 8, Q08006, doi:10.1029/2006GC001492.

Shu, L.S., 1991. The late Proterozoic terrane tectonics and collision orogenic belt in the north Jiangxi, eastern China. Ph.D. thesis, Nanjing University. p 212.

Shu, L.S., 2012. An analysis of principal features of tectonic evolution in South China Block. Geological Bulletin of China 31, 1035–1053.

Shu, L.S., Shi, Y.S., Guo, L.Z., 1995. Plate and terrane tectonics in the middle segment of Jiangnan orogenic belt and its collision orogenic dynamics. Nanjing University Publishing House, Nanjing, p 236.

Sillitoe, R.H., 2010. Porphyry copper systems. Economic Geology 105, 3–41.

Sillitoe, R.H., Mortensen, J.K., 2010. Longevity of porphyry copper formation at Quellaveco, Peru. Economic Geology 105, 1157–1162.

Steiger, R.H., Jäger, E., 1977. Subcommission on geochronology: convention on the use of decay constants in geo- and cosmochronology. Earth and Planetary Sciences Letters 36, 359–362.

Valencia, V.A., Ruiz, J., Barra, F., Geherls, G., Ducea, M., Titley, S.R., Ochoa-Landin, L., 2005. U–Pb zircon and Re–Os molybdenite geochronology from La Caridad porphyry copper deposit: insights for the duration of magmatism and mineralization in the Nacozari District, Sonora, Mexico. Mineralium Deposita 40, 175–191.

Von Quadt, A., Irena Peytcheva, I., Kamenov, B., Fanger, L., Heinrich, C.A., Frank, M., 2002. The Elatsite porphyry copper deposit in the Panagyurishte ore district, Srednogorie zone, Bulgaria: U–Pb zircon geochronology and isotope-geochemical investigations of magmatism and ore genesis. Geological Society, London, Special Publications 204, pp. 119–135.

Wang, C.Y., Li, X.F., Xiao, R., Bai, Y.P., Yang, F., Mao, W., Jiang, S.K., 2012. Elements mobilization of mineralized porphyry rocks during hydrothermal alteration at Zhushahong porphyry copper deposit, Dexing district, South China. Acta Petrologica Sinica 28, 3869–3886.

Wang, Q., Xu, J.F., Jian, P., Bao, Z.W., Zhao, Z.H., Li, C.F., Xiong, X.L., Ma, J.L., 2006. Petrogenesis of adakiic porphyries in an extensional tectonic setting, Dexing, South China: implications for the genesis of porphyry copper mineralization. Journal of Petrology 47, 119–144.

Wong, L., Davis, D.W., Hanes, J.A., Archibald, D.A., Hodgson, C.J., 1989. An integrated U–Pb and Ar–Ar geochronological study of the Archean Sigma gold deposit, Val D'Or, Quebec. Geological Association of Canada-Mineralogical Association of Canada Program with Abstract 14, 45.

Zhou, X.M., Li, W.X., 2000. Origin of late Mesozoic igneous rocks in southeastern China: implications for lithosphere subduction and underplating of mafic magmas. Tectonophysics 326, 269–287.

Zhou, X.M., Zhu, Y.H., 1993. Late Proterozoic collisional orogeny and geosuture in southeastern China: petrological evidence. Chinese Journal of Geochemistry 12 (3), 239–251.

Zhou, X.M., Sun, T., Shen, W.Z., Shu, L.S., Niu, Y.L., 2006. Petrogenesis of Mesozoic granitoids and volcanic rocks in South China: a response to tectonic evolution. Episodes 29, 26–33.

Zhu, X., Huang, C.K., Rui, Z.Y., 1983. Dexing porphyry copper deposit. Geological Publishing House, Beijing, 336 p.